The Evolution of Mercury's Crust: A Global Perspective from MESSENGER

Brett W. Denevi, *et al.*

Science **324**, 613 (2009);
DOI: 10.1126/science.1172226

This copy is for your personal, non-commercial use only.

If you wish to distribute this article to others, you can order high-quality copies for your colleagues, clients, or customers by clicking here.

Permission to republish or repurpose articles or portions of articles can be obtained by following the guidelines here.

The following resources related to this article are available online at www.sciencemag.org (this information is current as of July 13, 2010):

Updated information and services, including high-resolution figures, can be found in the online version of this article at:
http://www.sciencemag.org/cgi/content/full/324/5927/613

A list of selected additional articles on the Science Web sites **related to this article** can be found at:
http://www.sciencemag.org/cgi/content/full/324/5927/613#related-content

This article **cites 29 articles**, 8 of which can be accessed for free:
http://www.sciencemag.org/cgi/content/full/324/5927/613#otherarticles

This article has been **cited by** 4 article(s) on the ISI Web of Science.

This article has been **cited by** 2 articles hosted by HighWire Press; see:
http://www.sciencemag.org/cgi/content/full/324/5927/613#otherarticles

This article appears in the following **subject collections**:
Planetary Science
http://www.sciencemag.org/cgi/collection/planet_sci

Science (print ISSN 0036-8075; online ISSN 1095-9203) is published weekly, except the last week in December, by the American Association for the Advancement of Science, 1200 New York Avenue NW, Washington, DC 20005. Copyright 2009 by the American Association for the Advancement of Science; all rights reserved. The title *Science* is a registered trademark of AAAS.

the surface grows. Line plots of emission as functions of LOS distance behind the terminator (Fig. 2D) reveal a more rapid increase for Na than for Ca and Mg. This difference is consistent with the view that there is a substantial concentration of low-energy Na relative to Ca and Mg near the terminator.

In the fantail and near-terminator regions, emission rates were converted to approximate LOS abundances using column density factors (Table 1) calculated from *g* values (the emission probability per atom, expressed as photons s^{-1} $atom^{-1}$) for atoms at rest with respect to Mercury (*26*). These estimates indicate that although the average Na and Mg abundances measured by MASCS in the near-planet exosphere are comparable, those for Ca are smaller than Na by a factor of ~35 to 40. Because flyby observations do not provide complete coverage, it is not possible to determine whether these differences result from the relative amounts of Mg, Ca, and Na released to the exosphere or from differences in photoionization lifetimes and transport.

The detection of Mg in Mercury's exosphere is not a surprising result and supports the identification of Mg^+ in the planet's magnetosphere during MESSENGER's first flyby (*27*). Ground-based spectroscopic observations of the regolith indicate the presence of Mg-bearing minerals as well as those of Ca and Na (*28*). Additionally, analysis of global-scale color images obtained during the MESSENGER flybys argues for a substantial Mg component in Mercury's crust (*29*). Therefore, a considerable portion of the Mg in the exosphere must be derived from Mercury's surface materials (*15*, *19*, *20*). On the other hand, the differences in spatial distributions observed here, particularly those of the chemically similar elements Mg and Ca, were unexpected and remain unexplained.

References and Notes

1. W. H. Smyth, M. L. Marconi, *Astrophys. J.* **441**, 839 (1995).
2. A. E. Potter, R. M. Killen, T. H. Morgan, *Icarus* **186**, 571 (2007).
3. R. M. Killen, M. Sarantos, A. E. Potter, P. Reiff, *Icarus* **171**, 1 (2004).
4. A. L. Broadfoot, S. Kumar, M. J. S. Belton, M. B. McElroy, *Science* **185**, 166 (1974).
5. D. E. Shemansky, A. L. Broadfoot, *Rev. Geophys. Space Phys.* **15**, 491 (1977).
6. A. E. Potter, T. H. Morgan, *Science* **229**, 651 (1985).
7. A. E. Potter, T. H. Morgan, *Icarus* **67**, 336 (1986).
8. T. Bida, R. M. Killen, T. H. Morgan, *Nature* **404**, 159 (2000).
9. A. E. Potter, R. M. Killen, T. H. Morgan, *Meteorit. Planet. Sci.* **37**, 1165 (2002).
10. A. E. Potter, R. M. Killen, *Icarus* **194**, 1 (2008).
11. J. Baumgardner, J. Wilson, M. Mendillo, *Geophys. Res. Lett.* **35**, L03201, 10.1029/2007GL032337 (2008).
12. W. E. McClintock, M. R. Lankton, *Space Sci. Rev.* **131**, 481 (2007).
13. S. C. Solomon *et al.*, *Space Sci. Rev.* **131**, 3 (2007).
14. W. E. McClintock *et al.*, *Science* **321**, 62 (2008).
15. R. M. Killen *et al.*, *Space Sci. Rev.* **132**, 433 (2007).
16. W. F. Huebner, J. J. Keady, S. P. Lyon, *Astrophys. Space Sci.* **195**, 1 (1992).
17. M. Fulle *et al.*, *Astrophys. J.* **661**, L93 (2007).
18. A. L. Sprague *et al.*, *Icarus* **129**, 506 (1997).
19. R. M. Killen *et al.*, *J. Geophys. Res.* **106**, 20509 (2001).
20. F. Leblanc *et al.*, *Geophys. Res. Lett.* **35**, L18204, 10.1029/2008GL035322 (2008).
21. J. A. Slavin *et al.*, *Science* **321**, 85 (2008).
22. B. J. Anderson *et al.*, *Eos Trans. AGU* **89** (fall meeting suppl.), abstr. U12A-04 (2008).
23. J. A. Slavin *et al.*, *Science* **324**, 606 (2009).
24. M. Sarantos *et al.*, *Geophys. Res. Lett.* **36**, 10.1029/2008GL036207 (2009).
25. R. M. Killen, T. A. Bida, T. H. Morgan, *Icarus* **173**, 300 (2005).
26. R. M. Killen, D. E. Shemansky, N. Mouawad, *Astrophys. J.* **181** (suppl.), 351 (2009).
27. T. H. Zurbuchen *et al.*, *Science* **321**, 90 (2008).
28. A. L. Sprague *et al.*, *Planet. Space Sci.* **57**, 364 (2009).
29. B. W. Denevi *et al.*, *Science* **324**, 613 (2009).
30. We thank M. Lankton and M. Kochte for their important contributions to the acquisition and analysis of the data reported here. The MESSENGER project is supported by the NASA Discovery Program under contracts NAS5-97271 to Johns Hopkins University Applied Physics Laboratory and NASW-00002 to Carnegie Institution of Washington. R.J.V., R.M.K., and A.L.S. are supported by the MESSENGER Participating Scientist Program.

19 February 2009; accepted 8 April 2009
10.1126/science.1172525

The Evolution of Mercury's Crust: A Global Perspective from MESSENGER

Brett W. Denevi,[1]* Mark S. Robinson,[1] Sean C. Solomon,[2] Scott L. Murchie,[3] David T. Blewett,[3] Deborah L. Domingue,[3] Timothy J. McCoy,[4] Carolyn M. Ernst,[3] James W. Head,[5] Thomas R. Watters,[6] Nancy L. Chabot[3]

Mapping the distribution and extent of major terrain types on a planet's surface helps to constrain the origin and evolution of its crust. Together, MESSENGER and Mariner 10 observations of Mercury now provide a near-global look at the planet, revealing lateral and vertical heterogeneities in the color and thus composition of Mercury's crust. Smooth plains cover approximately 40% of the surface, and evidence for the volcanic origin of large expanses of plains suggests that a substantial portion of the crust originated volcanically. A low-reflectance, relatively blue component affects at least 15% of the surface and is concentrated in crater and basin ejecta. Its spectral characteristics and likely origin at depth are consistent with its apparent excavation from a lower crust or upper mantle enriched in iron- and titanium-bearing oxides.

Two close-approach flybys of Mercury (on 14 January 2008 and 6 October 2008) by the MESSENGER spacecraft, together with Mariner 10 observations, provide high-resolution images of 90% of this enigmatic planet's surface (*1*). These data permit a planet-wide assessment of the processes that shaped Mercury's crust: volcanism, deformation, and impact cratering. Crustal stresses play an important role in modulating and directing magmatic activity, impacts localize both volcanic and tectonic activity, and craters and ejecta provide our only probe deep into the crust. Here, we present a global catalog of the major geologic terrains and their stratigraphy and distribution across the surface, as well as an assessment of their implications for the formation and evolution of Mercury's crust.

MESSENGER's second flyby has confirmed the prediction (*2*), made on the basis of Mariner 10 images of less than half of Mercury's surface, that tectonic features on Mercury are dominantly contractional (*3*, *4*). Because a lithospheric stress state dominated by compression inhibits the ascent of magma, the timing of deformation recorded by lobate scarps (Fig. 1A) and other contractional landforms is important for understanding the history of volcanism on Mercury (*5*). The second MESSENGER flyby also reinforced the view that volcanism was an important process in Mercury's geologic history (*6*–*8*). Similar to features seen in images from the first flyby (*6*, *7*), spectrally distinct plains deposits (Fig. 2), lobate margins, crater embayment and flooding relationships, and wrinkle-ridge rings (Fig. 1A) provide evidence for widespread effusive volcanism. Rimless depressions surrounded by material of higher albedo and a steeper spectral slope (Fig. 1B) are additional candidates for sites of explosive volcanism (*6*, *7*).

MESSENGER's flybys have emphasized that first-order albedo and color contrasts on the planet are largely dominated by fresh crater materials. The second flyby revealed the rays and interiors of two large rayed craters, termed "A" and "B," that were first discovered with Earth-based radar (*9*). The rays of crater A (85 km in diameter and centered at 34°S, 12°E) extend approximately 1900 km, and those of crater B reach at least 4500 km (Fig. 1C). On the Moon, rays rarely exceed 2000 km in length (*10*). Rays of such great extent are thus unexpected on

---

[1] School of Earth and Space Exploration, Arizona State University, Tempe, AZ 85251, USA. [2] Department of Terrestrial Magnetism, Carnegie Institution of Washington, Washington, DC 20015, USA. [3] Johns Hopkins University Applied Physics Laboratory, Laurel, MD 20723, USA. [4] National Museum of Natural History, Smithsonian Institution, Washington, DC 20560, USA. [5] Department of Geological Sciences, Brown University, Providence, RI 02912, USA. [6] Center for Earth and Planetary Studies, National Air and Space Museum, Smithsonian Institution, Washington, DC 20560, USA.

*To whom correspondence should be addressed. E-mail: bdenevi@ser.asu.edu

Mercury, given the higher gravitational acceleration and comparatively limited extent of continuous ejecta deposits (*11*). Among the possible explanations for these findings are that the two Mercury craters are substantially younger than the lunar crater Tycho, ray material coalesces more efficiently to make distal rays more distinctive, space weathering on Mercury is less efficient at erasing rays than on the Moon, or ray material travels farther on Mercury than predicted. In addition to exposing fresh material, impact events also excavate material from depths as great as tens of kilometers below the surface, providing a means to assess vertical heterogeneities in the crust (Fig. 2).

The latest MESSENGER data confirm the presence on Mercury of albedo and color variations related to compositional heterogeneities (*8*). These variations are subtle compared with those of the Moon. Mercury shows variations smaller in relative reflectance of mature terrain than does the Moon (factor of 1.7 versus 2.6 at 750 nm) but larger than variations across the lunar highlands (1.1) or among major mare units (1.4). Multispectral images from the Mercury Dual Imaging System (MDIS) (*1*) and ultraviolet (UV)–visible–near-infrared (NIR) spectra from the Mercury Atmospheric and Surface Composition Spectrometer (MASCS) show that Mercury's major color units all share red-sloped reflectance spectra without strong crystal-field absorptions by iron-bearing silicates for both mature and immature materials (*12*, *13*) (Fig. 3A). Color variations among units are thus primarily products of changes in the steepness of the spectral slope (430 to 1020 nm), with steeper slopes termed relatively red and shallower slopes relatively blue.

Spectral slope, relative reflectance, and morphology distinguish three major terrain types (*13*) on Mercury: smooth plains, intermediate terrain (IT), and low-reflectance material (LRM). The second flyby color data demonstrate that these three terrains are broadly sufficient to describe the majority of Mercury's surface and allow further subdivision.

The smooth plains have a lower density of impact craters (*14*) and typically fill low-lying areas such as impact craters and basins. Their reflectance and spectral slope vary from unit to unit, and three subtypes are identified from global color data (Fig. 3A). High-reflectance red plains (HRP) are the most conspicuous of the smooth plains, with reflectances of up to 20% above the global mean and relatively steep spectral slopes. These plains typically display sharp color and morphologic boundaries with surrounding terrain (*6*, *13*). Intermediate plains (IP) have reflectance and color properties similar to the global mean. They also exhibit sharp morphologic boundaries with the surrounding terrain, as well as color boundaries where they overlie LRM. Low-reflectance blue plains (LBP) have reflectances 15% below the global mean and spectral properties intermediate to IP and LRM. A decrease in spectral slope of ~3% is observed from HRP to LBP.

The IT includes areas with a higher crater density than smooth plains and generally corresponds to regions mapped as heavily cratered terrain and intercrater plains from Mariner 10 images (*15*, *16*). The reflectance and color properties of the IT are similar to the global mean, although they show moderate variation.

The LRM exhibits reflectances as low as 30% below the global mean, and its spectral slope is ~5% lower than that of the HRP (Fig. 3A). At wavelengths below ~500 nm, spectra of the LRM exhibit a relative upturn, most clearly observed in ratioed MASCS spectra (*12*). The spectral properties of LRM are remarkably consistent and show little change whether they are freshly exposed in crater ray deposits or have been long exposed to the space-weathering environment on the surface. LRM occurs as broad regions with diffuse margins as well as in concentrated "centers" typically comprised of crater or basin ejecta. The LRM does not exhibit distinctive morphologic characteristics; it includes terrain that would typically be mapped as IT, were it not for its color properties.

We created enhanced color images from 11-band, photometrically corrected wide-angle camera (WAC) (*1*) mosaics (0.5 to 5.0 km per pixel) and combined the second principal component, first principal component, and 430/1000–nm ratio into red-green-blue composite images (Fig. 4A) (*13*). The second principal component largely removes the spectral effects of maturity, so that the red-blue planes encode compositional variations in the surface material, whereas the green plane is dominated by maturity variations and therefore highlights fresh craters. Together with narrow-angle camera (NAC) (*1*) high-resolution (0.3 to 0.5 km per pixel) images, these products allow near-global mapping on the basis of both color and morphology. Areas of MDIS mosaics with high Sun illumination, which is disadvantageous for viewing topography and texture, were supplemented with Mariner 10 images (1 km per pixel) (*17*) where available; otherwise, these high-Sun-illumination areas were excluded.

These data demonstrate that smooth plains are widespread on Mercury: They cover ~40% of the surface and are globally distributed (Fig. 4B). On the basis of Mariner 10 images, estimates for the areal extent of smooth plains varied from 15 to 40% (*2*, *18*). Individual deposits range from hundreds of square kilometers to 1.7 million km^2 (the Caloris basin interior plains), rivaling the sizes of the largest flood basalt units on the Earth or Moon. The majority of smooth plains are probably of volcanic origin (*2*, *6*), although impact melt and basin ejecta are likely explanations for a subset of plains units. Vast expanses of smooth plains deposits with features that are diagnostic of volcanically emplaced materials

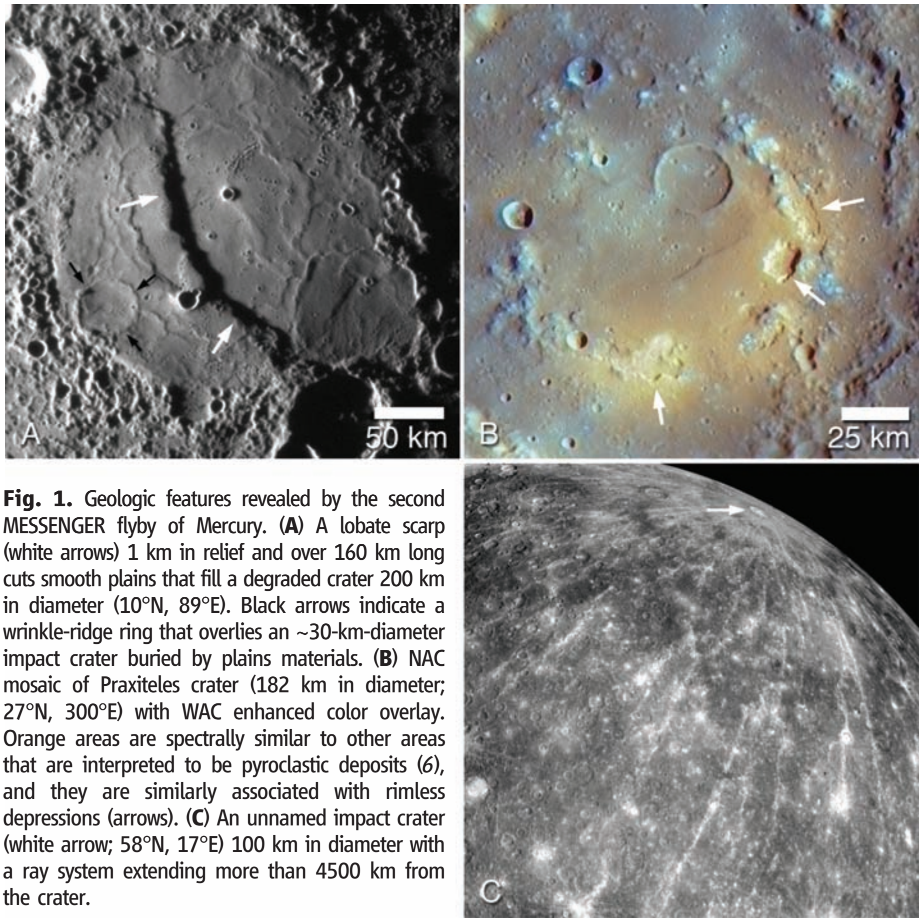

Fig. 1. Geologic features revealed by the second MESSENGER flyby of Mercury. (**A**) A lobate scarp (white arrows) 1 km in relief and over 160 km long cuts smooth plains that fill a degraded crater 200 km in diameter (10°N, 89°E). Black arrows indicate a wrinkle-ridge ring that overlies an ~30-km-diameter impact crater buried by plains materials. (**B**) NAC mosaic of Praxiteles crater (182 km in diameter; 27°N, 300°E) with WAC enhanced color overlay. Orange areas are spectrally similar to other areas that are interpreted to be pyroclastic deposits (*6*), and they are similarly associated with rimless depressions (arrows). (**C**) An unnamed impact crater (white arrow; 58°N, 17°E) 100 km in diameter with a ray system extending more than 4500 km from the crater.

(*2*, *6*, *7*, *18*) demonstrate that volcanism was extensive on Mercury. In many areas, a sequence of several generations of smooth plains can be observed, and crater excavation relationships demonstrate that smooth plains can be as thick as 5 km (*6*, *19*). The globally distributed intercrater plains of the IT may simply be older and more degraded smooth plains that formed through widespread volcanism during or at the end of the late heavy bombardment (*16*); however, emplacement as basin ejecta remains a possibility (*20*).

Observations from the second MESSENGER flyby confirm that the LRM is a key terrain type (*13*): It covers at least 15% of Mercury, and individual regions of LRM can be greater than 4 million km^2 in extent (Fig. 4). Because of the diffuse nature of regional LRM deposits, most LRM boundaries are mapped as approximate. At least 65 craters and basins greater than 20 km in diameter exhibit some form of LRM ejecta, implying depths of origin of the LRM from several kilometers to as much as 25 km. The association with impact crater and basin ejecta and the observation that regional LRM deposits are often without clear morphologic boundaries (aside from distinct margins in crater and basin ejecta, or where embayed by smooth plains) and occur as thin surficial deposits in many locations indicate a subsurface origin through impact excavation and subsequent distribution across the surface as an ejecta veneer (Fig. 2). Thus, LRM source material appears to originate at depth and may represent a component of the lower crust or upper mantle that was redistributed on the surface. However, the absence of LRM in the ejecta of many large impact craters demonstrates heterogeneous distribution of its source material throughout the crust both horizontally and vertically (Fig. 3B). In some cases, diffuse LRM deposits may have originally been magmatically emplaced as intrusive or extrusive deposits, now degraded and mixed through impact processes.

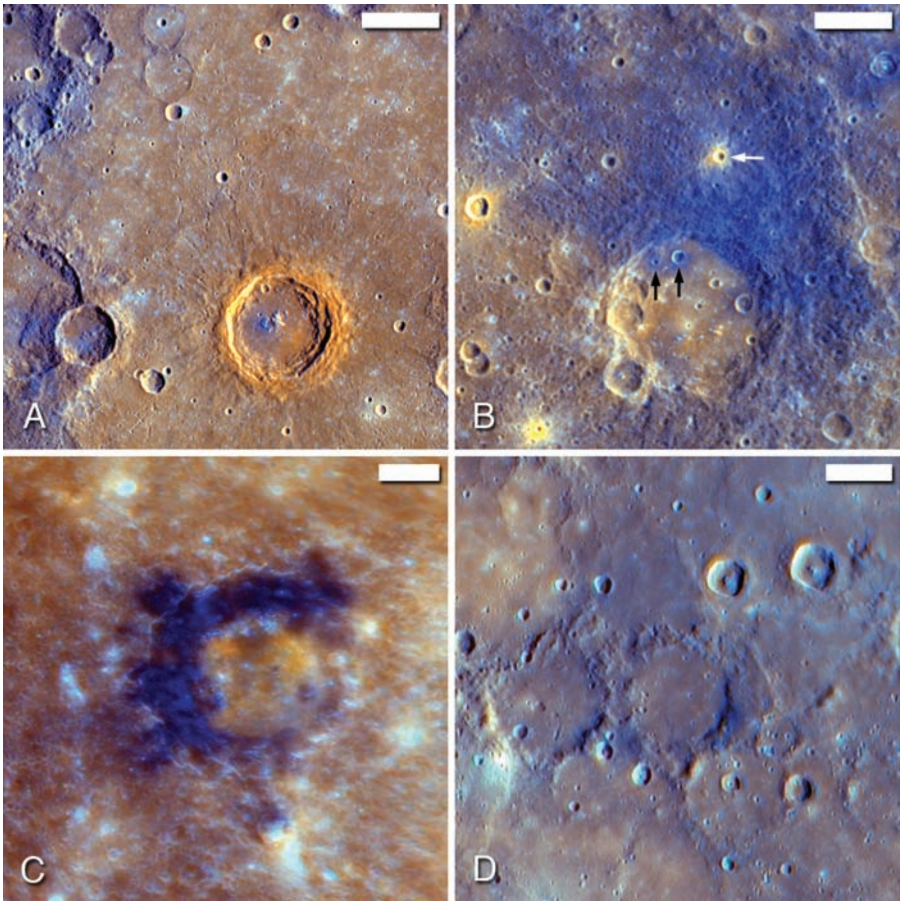

Fig. 2. Key stratigraphic relationships observed by MDIS. (A) and (B) show portions of the highest-resolution color images (462 m per pixel); (C) and (D) are composites of NAC and WAC mosaics. **(A)** Smooth plains fill a degraded basin near the crater Rudaki (image centered at 4°S, 304°E). The ejecta of the 68-km-diameter crater near the center has an elevated albedo and steeper spectral slope than the surrounding plains, suggesting that the surface layer of IP buried an HRP unit exposed by this crater. Portions of the central peak have exhumed LRM from an estimated depth (*38*) of 7 to 10 km. **(B)** Crater Titian (121 km in diameter; 4°S, 317°E) excavated LRM from beneath smooth plains; this LRM ejecta masks the spectral character of older smooth plains, except where small craters re-expose plains material (white arrow). Younger smooth plains fill Titian, and small impacts expose LRM from below these plains (black arrows). **(C)** LRM center in unnamed crater (165 km in diameter; 9°S, 20°E). The asymmetrical distribution of LRM exposed by impact craters is common. **(D)** LBP northwest of Caloris basin (43°N, 121°E). The LBP are spectrally indistinguishable from the older craters they embay and do not have a sharp morphologic boundary with IP/HRP. Within the LBP, large impact craters typically do not have spectrally distinct ejecta [as opposed to those in (A) to (C)]. All scale bars are 50 km.

The relationship between the diffuse LRM deposits and LBP is complex. In some places, LRM ejecta constitute a thin surface coating on HRP or IP, masking the inherent color properties of the plains (Fig. 2B). The circum-Caloris plains, the largest expanse of LBP, are also the most complicated. Several observations imply a relationship with Caloris ejecta: The plains generally have no distinct boundaries with the hummocky plains of the Odin Formation (interpreted to be basin ejecta); radially away from Caloris, they are often interfingered with IP/HRP; in portions of their distal margins, they have no distinct morphologic or color boundaries and grade into HRP; and in some areas with distinct morphologic boundaries, their color properties are indistinguishable from the terrain they embay (Fig. 2D) (*7*, *13*). However, crater counts indicate that they are younger than the Caloris interior plains, which in turn are younger than Caloris rim materials (*14*, *21*), and thus these LBP are interpreted to be the result of later resurfacing that was potentially of volcanic origin (*14*, *21*). These conflicting observations must be reconciled before the nature of the LBP can be confidently understood.

The widespread distribution of smooth plains that are interpreted to be of volcanic origin demonstrates that the global compressive lithospheric stresses indicated by lobate scarps did not preclude extensive volcanism at least until well after the formation of the Caloris basin. Wrinkle ridges and lobate scarps (Fig. 1A) in many smooth plains units suggest that contractional deformation continued after the emplacement of the youngest volcanic plains (*4*). Understanding the ascent and eruption of magma requires knowledge of the mechanical structure and the evolution of stress both globally and locally as well as the density and thickness of the crust and of mantle-derived magmas (*5*, *22*). Observations to date make it difficult to place precise constraints on these parameters, although current compositional interpretations argue against a large density contrast between Mercury's crust and upper mantle.

The interpretation of MDIS color units in terms of lithologic units poses a challenge. Earth-based reflectance spectra (*23*), confirmed by MESSENGER observations of mature and immature material (*12*, *13*), show no 1-µm absorption band, implying a low (<6 weight percent) ferrous iron (FeO) content of silicate minerals (*23*, *24*). Thermal emission measurements at microwave wavelengths (0.3 to 20.5 cm) indicate that Mercury's surface is 40% more transparent than the lunar highlands (*25*). These two observations have led to the inference that

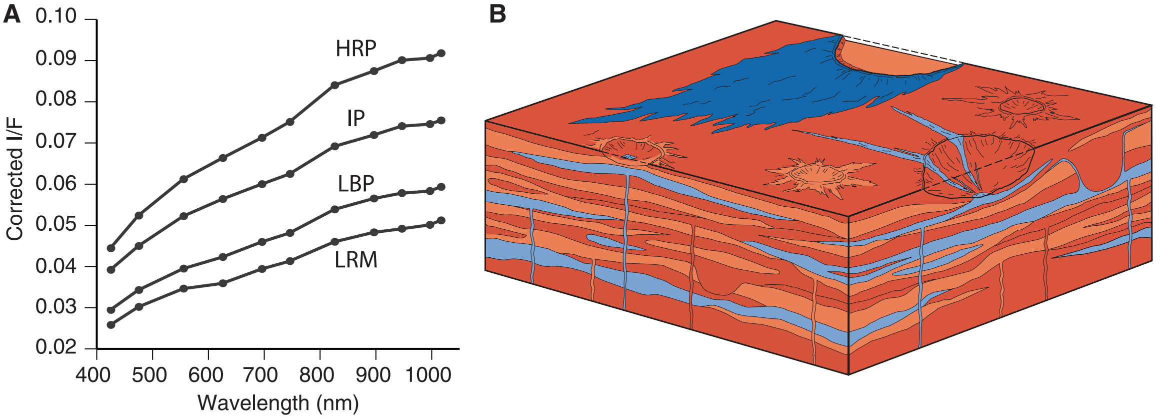

Fig. 3. (**A**) MDIS spectra (photometrically corrected to an incidence angle of 30° and an emission angle of 0°, both measured from the vertical) of the three type examples of smooth plains and the LRM. I/F (radiance factor, known as reflectance) is the observed radiance divided by the expected radiance from a normally solar-illuminated Lambertian surface. Remaining uncertainties in the calibration contribute to the small wiggles seen in these spectra. (**B**) Schematic of the complex vertical and lateral heterogeneities expected as a result of the accumulation of Mercury's crust through extrusive and intrusive volcanism over time. Colors show the compositional variation among HRP (light orange), IP (dark orange), LBP (light blue) deposits, and LRM centers (dark blue). The sectioned crater on the left depicts a possible origin for color variations, such as those of Fig. 2A. Rim materials excavate buried HRP, and the central peak exposes buried LBP. The sectioned crater on the right shows the morphology of LRM streamers, such as those of Mozart crater, which may be due to the excavation of LRM or LBP (see also Fig. 2, B and C). In the background are continuous LRM ejecta (dark blue) and lava fill of the basin as observed at Tolstoj basin, illustrating the proposed origin of LRM centers as excavated components of the lower crust or upper mantle relatively enriched in the proposed low-reflectance mineral. This diagram is simplified, and more vertical mixing is expected through intrusions of rising magma, such as dikes and sills (*6*), and impacts of various sizes throughout the crustal formation process. The illustration is not to scale.

Mercury's crust contains lower abundances of iron (Fe) plus titanium (Ti) than the lunar highlands (*23*–*25*). However, Mercury's average reflectance is similar to, or lower than, the reflectance of the integrated lunar nearside (*26*), 30% of which is covered by high-Fe, high-Ti basalts. Mercury's reflectance cannot be ascribed solely to differential space weathering of a lunarlike anorthositic crust, because immature materials on Mercury are also as much as 30% lower in reflectance than comparable material on the Moon (*13*, *17*). This result indicates that Mercury's crust is not dominantly anorthositic but instead possibly rich in low-Fe pyroxene or olivine (both of which have reflectances lower than that of anorthite) and a spatially variable low-reflectance component. During MESSENGER's second Mercury flyby, MASCS observations detected magnesium (Mg) in the exosphere, a result that requires a substantial source of Mg at Mercury's surface (*27*), such as magnesian pyroxene.

The lack of a 1-µm band, the presence of the spatially variable LRM, and Mercury's overall low albedo imply the presence of an opaque phase (*28*, *29*), and iron, titanium, and carbon are the most cosmochemically abundant elements that contribute to strong absorptions at UV-through-NIR wavelengths. Carbon is unlikely to be responsible because it is effectively sequestered to the core during early planetary differentiation (*30*) and lost through volatilization in volcanic eruptions. Ti alone is not highly absorbing at visible-NIR wavelengths unless it is paired with another transition metal, such as Fe; Fe alone is typically red-sloped or exhibits a 1-µm band if contained in silicates. In oxide minerals, Fe and Ti together have a strong, broad, charge-transfer absorption that results in low reflectance and a neutral spectrum, in some cases with a shallow upturn at short wavelengths. Thus, opaque Fe- and Ti-bearing minerals such as ilmenite ($FeTiO_3$), or possibly any oxide with considerable abundances of Fe and Ti (*31*), match the spectral characteristics of the LRM. To estimate potential abundances of Fe- and Ti-bearing oxides, we used a radiative transfer model based on the equations of Hapke (*32*). Spectra were converted to single-scattering albedo (the probability of a photon being scattered by a particle), and HRP spectra were mixed linearly with ilmenite spectra (used as a proxy for any Fe- and Ti-bearing oxide) so as to match the characteristics of the IP and LRM. Up to 15% ilmenite is required to match MDIS spectra of the IT, and up to 40% ilmenite is needed for spectra of the most extreme LRM center (a portion of the Tolstoj basin annulus). These abundances are maximum values because of the assumption that all of the decrease in reflectance is due to ilmenite.

The maximum ilmenite abundance required to match intermediate terrain is consistent with MESSENGER's Neutron Spectrometer measurements, which observed predominantly intermediate terrain and are interpreted as indicating abundances of neutron-absorbing elements (Fe, Ti, gadolinium, samarium) within the range of lunar soil samples from Luna 16 to Luna 24 (*33*). These soils contain moderate to high abundances of Fe and Ti, which if contained predominantly in oxide minerals would explain their high abundance without a corresponding 1-µm band. Early crystallization of Fe- and Ti-bearing oxides such as ilmenite under reducing conditions (near the iron-wüstite buffer) from a Ti-rich and relatively FeO-poor melt limits FeO incorporation into later-crystallizing pyroxene (*34*). In such an environment, Mg-calcium–bearing pyroxenes would be expected to form after substantial amounts of ilmenite crystallize. High abundances of Fe and/or Ti are contrary to the inferences from Earth-based microwave measurements (*25*). However, the interpretation of the microwave data also predicts that Mercury's albedo is higher than that of the lunar highlands (*25*), which is not observed (*26*). Earth-based photometric observations indicate that Mercury's regolith is more backscattering than the average lunar terrain; its scattering properties (typically related to opaque content) are more similar in character to lunar maria than to lunar highlands (*26*). Radar observations indicate that LRM centers, such as the Tolstoj annulus, show low radar returns similar to the lunar maria and in contrast to HRP, which is consistent with a higher Fe and Ti content in LRM (*9*).

Such high abundances of ilmenite (or any Fe- and Ti-bearing oxide) for the LRM are improbable for extrusive volcanic rocks and are more plausible if the LRM material originates from cumulate deposits. Such cumulates can form as late-stage products of a large-scale magma ocean or from crystal-liquid fractionation within subsurface magma chambers. These modes of occurrence are consistent with the stratigraphy of LRM deposits that are exposed on the surface by impact excavation. The smooth plains materials, containing a smaller fraction of dense Fe- and Ti-bearing oxides, would be more likely to reach the surface in volcanic eruptions (*5*, *22*).

The global view of Mercury indicates that widespread resurfacing probably obscured early events in the planet's geological history. Evidence for large-scale volcanic deposits several kilometers thick (*6*, *7*, *19*) suggests that a substantial volume of the crust was created through repeated volcanic eruptions. Basins such as Caloris, filled nearly to their rims both inside and out, hint at the probable existence of older basins that are not yet recognized because of volcanic burial and impact degradation. Little evidence is found for an ancient feldspar-rich flotation crust such as that of the lunar high-

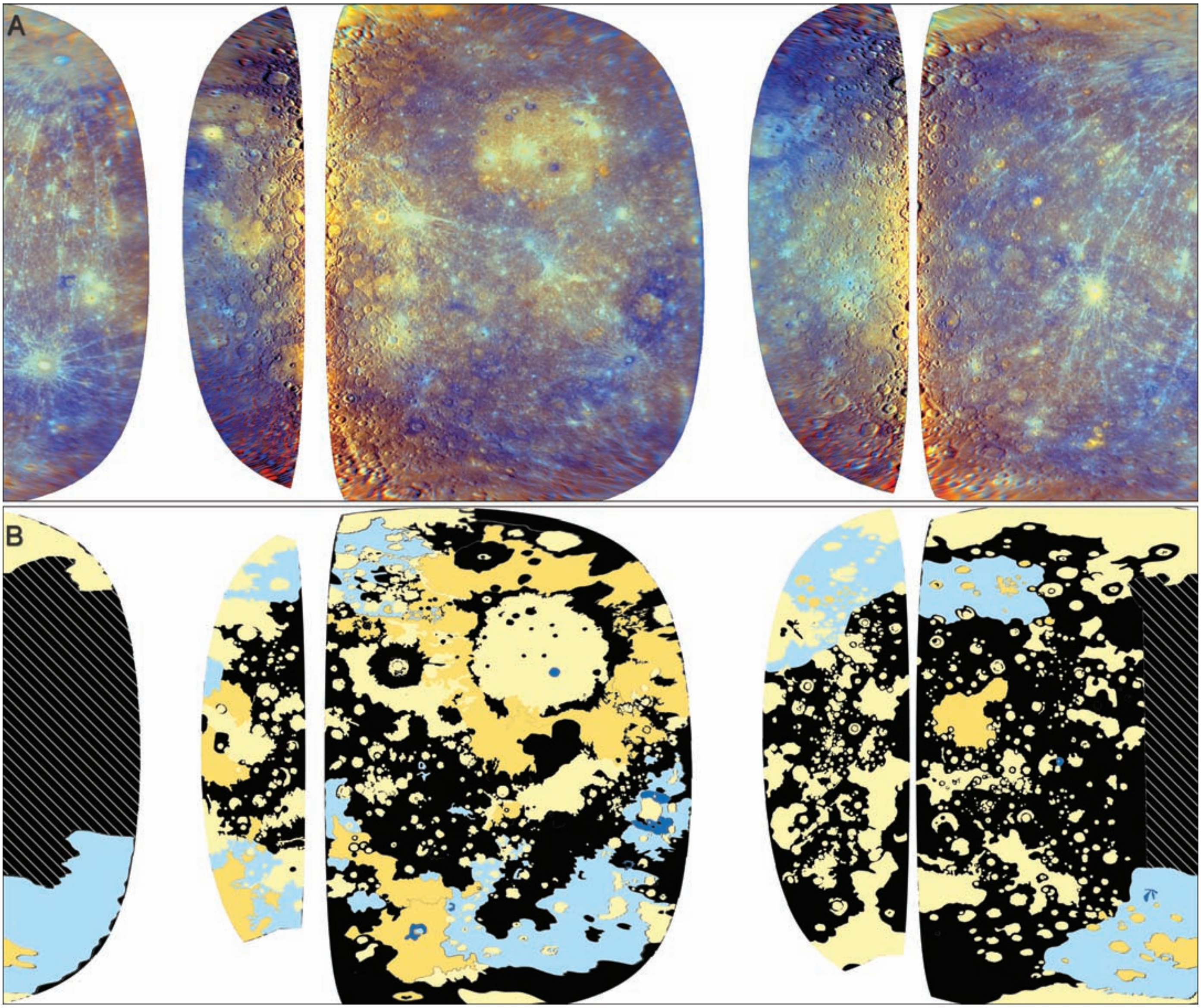

Fig. 4. Two simple cylindrical views of Mercury over ±75° latitude, 0° to 360°E longitude. (**A**) Enhanced color MDIS WAC mosaics. Areas in white are regions not yet imaged by MESSENGER. (**B**) Geologic map of Mercury from MESSENGER WAC and NAC mosaics and Mariner 10 clear-filter mosaics. Light yellow, HRP and IP; dark yellow, LBP; light blue, regional LRM; dark blue, LRM center; black, other (fresh crater ejecta or IT); and white, no data. Crosshatches indicate areas not mapped because of high Sun illumination. Areas near the terminator in (A) appear unnaturally red; until the final WAC calibration is available, color distinctions are subject to revision.

lands, which is thought to be the result of the crystal-liquid fractionation of a global magma ocean. If such an early crust existed, it may now be buried by younger volcanic material, but there is no definitive indication that feldspar-rich material has been excavated from depth. Removal of Mercury's earliest crust by a giant impact or vaporization in a hot solar nebula has been proposed to account for Mercury's high bulk density (*35*, *36*). If such an event occurred, crustal formation continued thereafter, most likely obscuring any record of early crustal stripping. The main inference from the combined MESSENGER data are that much of Mercury's crust formed as a result of the eruptions of magmas of varying composition over an extended duration of geologic time.

References and Notes

1. MESSENGER images were acquired with the MDIS, which includes the 11 filters (430 to 1020 nm) of the WAC and the monochrome (750 nm) NAC described in (*37*).
2. R. G. Strom, N. J. Trask, J. E. Guest, *J. Geophys. Res.* **80**, 4062 (1975).
3. S. C. Solomon *et al.*, *Science* **321**, 59 (2008).
4. T. R. Watters *et al.*, *Earth Planet. Sci. Lett.*, 10.1016/j.epsl.2009.01.015 (2009).
5. S. C. Solomon, *Geophys. Res. Lett.* **5**, 461 (1978).
6. J. W. Head *et al.*, *Science* **321**, 69 (2008).
7. S. L. Murchie *et al.*, *Science* **321**, 73 (2008).
8. M. S. Robinson, P. G. Lucey, *Science* **275**, 197 (1997).
9. J. K. Harmon *et al.*, *Icarus* **187**, 374 (2007).
10. R. B. Baldwin, *The Measure of the Moon* (Univ. of Chicago Press, Chicago, 1963).
11. D. E. Gault, J. E. Guest, J. B. Murray, D. Dzurisin, M. C. Malin, *J. Geophys. Res.* **80**, 2444 (1975).
12. W. E. McClintock *et al.*, *Science* **321**, 62 (2008).
13. M. S. Robinson *et al.*, *Science* **321**, 66 (2008).
14. R. G. Strom, C. R. Chapman, W. J. Merline, S. C. Solomon, J. W. Head III, *Science* **321**, 79 (2008).
15. N. J. Trask, J. E. Guest, *J. Geophys. Res.* **80**, 2461 (1975).
16. M. C. Malin, *Geophys. Res. Lett.* **3**, 581 (1976).
17. B. W. Denevi, M. S. Robinson, *Icarus* **197**, 239 (2008).
18. P. D. Spudis, J. E. Guest, in *Mercury*, F. Vilas, C. R. Chapman, M. S. Mathews, Eds. (Univ. of Arizona Press, Tucson, 1988), pp. 118–164.
19. C. M. Ernst, S. L. Murchie, O. S. Barnouin-Jha, M. S. Robinson, B. W. Denevi, *Lunar Planet. Sci.* **40**, abstr. 1900 (2009).
20. D. E. Wilhelms, *Icarus* **28**, 551 (1976).
21. C. I. Fassett *et al.*, *Lunar Planet. Sci.* **40**, abstr. 1889 (2009).
22. J. W. Delano, *Proc. Lunar Planet. Sci. Conf.* **20**, 3 (1990).
23. F. Vilas, in *Mercury,* F. Vilas, C. R. Chapman, M. S. Matthews, Eds. (Univ. of Arizona Press, Tucson, 1988), pp. 59-76.
24. D. T. Blewett, B. R. Hawke, P. G. Lucey, *Meteorit. Planet. Sci.* **37**, 1245 (2002).
25. D. L. Mitchell, I. de Pater, *Icarus* **110**, 2 (1994).
26. J. Warell, *Icarus* **167**, 271 (2004).

27. W. E. McClintock *et al.*, *Science* **324**, 610 (2009).
28. B. Rava, B. Hapke, *Icarus* **71**, 397 (1987).
29. D. T. Blewett *et al.*, *Earth Planet. Sci. Lett.*, 10.1016/j.epsl.2009.02.021 (2009).
30. V. J. Hillgren, C. K. Gessman, J. Li, in *Origin of the Earth and Moon*, R. M. Canup, K. Righter, Eds. (Univ. Arizona Press, Tucson, 2000), pp. 245–263.
31. M. A. Riner, P. G. Lucey, S. J. Desch, F. M. McCubbin, *Geophys. Res. Lett.* **36**, L02201 (2009).
32. B. Hapke, *Theory of Reflectance and Emittance Spectroscopy: Topics in Remote Sensing 3* (Cambridge Univ. Press, New York, 1993).
33. D. J. Lawrence, W. C. Feldman, J. O. Goldsten, *Lunar Planet. Sci.* **40**, abstr. 1761 (2009).
34. T. M. Usselman, G. E. Lofgren, C. H. Donaldson, R. J. Williams, *Proc. Lunar Sci. Conf.* **6**, 997 (1975).
35. A. G. W. Cameron, *Icarus* **64**, 285 (1985).
36. W. Benz, W. L. Slattery, A. G. W. Cameron, *Icarus* **74**, 516 (1988).
37. S. E. Hawkins III *et al.*, *Space Sci. Rev.* **131**, 247 (2007).
38. M. J. Cintala, R. A. F. Grieve, *Meteorit. Planet. Sci.* **33**, 889 (1998).
39. We gratefully acknowledge the MESSENGER engineers and technical support team. N. Laslo, H. Kang, R. Vaughan, A. Harch, R. Shelton, and A. Berman designed the imaging sequences used here. S. Turner, K. Becker, and C. Hash contributed to data calibration and processing. The MESSENGER project is supported by the NASA Discovery Program under contracts NAS5-97271 to the Johns Hopkins University Applied Physics Laboratory and NASW-00002 to the Carnegie Institution of Washington.

12 February 2009; accepted 8 April 2009
10.1126/science.1172226

Evolution of the Rembrandt Impact Basin on Mercury

Thomas R. Watters,[1]* James W. Head,[2] Sean C. Solomon,[3] Mark S. Robinson,[4] Clark R. Chapman,[5] Brett W. Denevi,[4] Caleb I. Fassett,[2] Scott L. Murchie,[6] Robert G. Strom[7]

MESSENGER's second Mercury flyby revealed a ~715-kilometer-diameter impact basin, the second-largest well-preserved basin-scale impact structure known on the planet. The Rembrandt basin is comparable in age to the Caloris basin, is partially flooded by volcanic plains, and displays a unique wheel-and-spoke–like pattern of basin-radial and basin-concentric wrinkle ridges and graben. Stratigraphic relations indicate a multistaged infilling and deformational history involving successive or overlapping phases of contractional and extensional deformation. The youngest deformation of the basin involved the formation of a ~1000-kilometer-long lobate scarp, a product of the global cooling and contraction of Mercury.

Impact basins, generally in excess of several hundred kilometers in diameter, are among the most important landforms created early in planetary history (*1*). Because of their typically ancient ages, most basins have been modified and filled with volcanic plains, which obscure their initial state and early evolution. A few basins, such as Orientale on the Moon, remain largely unfilled and provide substantial insight into basin formation and early modification (*2*, *3*). During its second flyby of Mercury in October 2008, the MESSENGER spacecraft imaged ~30% of the planet not previously seen by spacecraft. These images revealed a relatively unmodified basin centered near 33°S, 88°E (Fig. 1A). The interior of the basin, recently named Rembrandt, differs considerably from that of the well-preserved and larger Caloris basin, imaged by Mariner 10 (*4*, *5*) and during MESSENGER's first Mercury encounter (*6*–*11*). The Caloris basin contains substantial infill by plains of volcanic origin that cover its entire floor. On the basis of MESSENGER observations, we here assess the characteristics of the Rembrandt basin and their geological implications.

The Rembrandt basin (Fig. 1A) has a topographically distinct main rim crest made up of rugged, high-relief, inward-facing scarps and massifs. At ~715 km, its mean rim crest diameter is larger than the intermediate-scale, partly filled impact basins Beethoven (~625 km) and Tolstoj (~510 km) (*5*) and about half the size of the largest known basin, Caloris (>1500 km) (*7*, *8*). Numerous large impact craters are superposed on the rim of the basin (Fig. 1A). The number of craters ≥20 km in diameter per million square kilometers is not distinguishable from that for the rim of the Caloris basin [see supporting online material (SOM), figs. S1 to S3]. The crater size-frequency distribution (SFD) for the Rembrandt basin rim (Fig. 1B) is also similar to that for the Caloris basin rim (*11*). These results suggest that Rembrandt, like Caloris, is one of the youngest basins on Mercury, younger than Tolstoj and Beethoven, yet sufficiently old to show the pattern of fewer small-diameter craters relative to large-diameter craters that is characteristic of terrains formed before the end of the late heavy bombardment of the inner solar system (~3.9 billion years ago) (*12*).

Exterior to the basin rim crest are blocky and radially lineated ejecta deposits, well preserved to the north and northeast of the basin rim, respectively (Fig. 1, A and C). These deposits are comparable to the annuli of radially textured ejecta outside the rims of the Caloris basin (*5*, *11*) and the lunar Orientale basin (*2*, *3*). Basin interior units include a hummocky unit and a smooth plains unit. The hummocky unit extends inward from the basin rim by up to ~130 km (Fig. 1D) and is distinguished by knobs that rise up to hundreds of meters (from shadow measurements) above patches of rolling hills near the basin margin (Fig. 1C). This unit forms a discontinuous ring in the basin interior, confined to the northern margin. Two large, angular blocks or massifs on the southern edge of the hummocky unit have a maximum relief of >1.5 km (Fig. 1D). The inner edge of the hummocky unit and the massifs may mark the remnants of a ringlike structure with a diameter of ~450 km (Figs. 1 and 2). The hummocky and domical morphology of the unit and its position just inside the basin rim are similar to those of the Montes Rook Formation in Orientale, interpreted to have been formed by collapse and inward translation of the transient cavity rim and modification of radially textured rim deposits into domical blocks (*2*, *3*). This interpretation is supported by remnant radial crater-chain–like structures (Fig. 1D), similar to occurrences in Orientale, and suggests that the inner edge and massifs of this unit delineate the remnant of the transient cavity rim (*2*).

Smooth plains constitute the most areally extensive unit in the Rembrandt basin; occupy much of the basin interior; and extend to the southern, eastern, and parts of the western rim (Fig. 2A). In the lunar Orientale basin, non-mare smooth and rough plains inside the transient cavity are interpreted to be impact melt (*1*–*3*). On the basis of laboratory experiments and theoretical scaling arguments, the volume of impact melt formed in basins is predicted to increase with basin size and perhaps even to fill entirely the basin interior at the largest diameters (*13*). If the regional plains are impact melt, they would have been emplaced in the immediate aftermath of basin formation and collapse, before formation of any subsequent major impact craters, as has been documented for the lunar Orientale basin (*14*). Furthermore, they should have spectral characteristics appropriate for a physical mixture of the target materials.

Broadly distributed spectral units on Mercury identified from global principal component analysis and spectral ratios of MESSENGER's 11-color wide-angle camera (WAC) images include low-reflectance material (LRM), spectrally intermediate terrain, and three types of smooth plains: (i) high-reflectance red plains (HRP), (ii) intermediate plains, and (iii) low-reflectance blue plains (LBP) (*10*, *15*). Comparison of color data between the Rembrandt basin and other regions of the planet is complicated by the area's near-

---

[1]Center for Earth and Planetary Studies, National Air and Space Museum, Smithsonian Institution, Washington, DC 20560, USA. [2]Department of Geological Sciences, Brown University, Providence, RI 02912, USA. [3]Department of Terrestrial Magnetism, Carnegie Institution of Washington, Washington, DC 20015, USA. [4]School of Earth and Space Exploration, Arizona State University, Tempe, AZ 85251, USA. [5]Southwest Research Institute, 1050 Walnut Street, Boulder, CO 80302, USA. [6]Johns Hopkins University Applied Physics Laboratory, Laurel, MD 20723, USA. [7]Lunar and Planetary Laboratory, University of Arizona, Tucson, AZ 85721, USA.

*To whom correspondence should be addressed. E-mail: watterst@si.edu